mater.scichina.com link.springer.com

Published online 25 March 2024 | https://doi.org/10.1007/s40843-023-2853-0
Sci China Mater 2024, 67(4): 1217–1224

SPECIAL TOPIC: Computation-assisted Materials Screening and Design

Achieving surface and bulk rate matching for chemical looping partial oxidation of methane by modulating oxygen transport

Tingting Yang[1], Ran Luo[1], Xiangcheng Shi[1,5], Xianhua Zhang[1], Shican Wu[1], Chunlei Pei[1], Zhi-Jian Zhao[1,2,3*] and Jinlong Gong[1,2,3,4,5]

ABSTRACT **Chemical looping partial oxidation of methane (CL-POM) offers a promising approach to produce syngas with high selectivity and reduced explosion risk. However, the design of metal oxide oxygen carriers with excellent performance and continuous oxygen release capacity remains a challenge. In this study, we developed a composite oxygen carrier ($LaFeO_{3-\delta}/Ca_{1-\eta}Sr_{\eta}MnO_3$) with the aim of modulating the oxygen transport capacity of $Ca_{1-\eta}Sr_{\eta}MnO_3$ to maintain active structures on the $LaFeO_{3-\delta}$ (121) defected surface, thereby enhancing the activity and selectivity of CL-POM. The Fe-$O_4(O_V)$ and Fe-$O_3(O_V)_2$ local structures were found to serve as active sites for methane oxidation on the $LaFeO_{3-\delta}$ (121) defected surface, with comparable free energy barriers of reaction (ΔG_a = 1.44 and 1.40 eV, respectively). Based on the oxygen migration energy barriers and reaction energy barriers calculated by DFT, we determined oxygen transport coefficients and surface reaction rate constants to further assess the degree of rate matching between bulk oxygen transport and surface oxygen consumption. Finally, $LaFeO_{3-\delta}/Ca_{0.75}Sr_{0.25}MnO_3$ was proposed as a potential candidate for CL-POM. This composite material achieves commendable rate matching between surface reactivity and bulk oxygen transport, and notably exhibits the highest phase transition energy barrier, effectively inhibiting adverse phase transitions.**

Keywords: chemical looping technique, partial oxidation of methane, steady-state approximation, oxygen transport capacity, rate match

INTRODUCTION

Methane reforming has attracted widespread attention for the production of high-value chemicals and fuels [1–3]. Compared with steam methane reforming (SMR) and dry reforming of methane (DRM), partial oxidation of methane (POM) offers several advantages such as an exothermic process, low energy consumption, a reduced carbon footprint, and a rapid oxidation reaction rate [4–6]. Additionally, POM products can be used directly in the Fischer–Tropsch reaction due to the favorable H_2/CO ratio of 2 [7–10]. However, POM faces challenges related to its high production cost and the explosion risk associated with the use of pure oxygen [11,12]. To address these issues, chemical looping POM (CL-POM) has emerged as an alternative method that allows to achieve efficient energy conversion and reduce the cost of product separation [13–15].

The properties of oxygen carriers (OCs) significantly affect the activity and selectivity of CL-POM [16,17]. Among various factors, surface oxygen vacancies (OVs) in OCs have been shown to be advantageous for modulating the activity of surface lattice oxygen atoms, thereby enhancing the syngas selectivity [18–20]. However, existing strategies to promote the formation of OVs in OCs, including ion doping [20–22] and partial reduction of OCs [18,23], often result in the formation of OVs both on the surface and in the bulk of OCs, leading to a reduction in the oxygen release capacity and an accelerated onset of phase transition (to form a less reactive phase). These factors present challenges, hindering continuous progress in CL-POM [23–26].

In contrast, an alternative approach involves utilizing a different OC as a separate oxygen supplier (OS) to transport bulk oxygen atoms to the defected surface. By doing so, bulk oxygen transport and surface reactions can be effectively separated [23,27,28]. The modulation of surface structures can be achieved by adjusting the oxygen transport capacity of the OS, which directly impacts reaction performance. When the bulk oxygen transport rate surpasses or falls below the surface reaction rate, it can lead to undesired accumulation of active lattice oxygen atoms or OVs on the surface, resulting in either complete oxidation of methane or methane cracking [19,20,29]. Achieving a rate matching between bulk oxygen transport and surface reactions is therefore crucial. It ensures the preservation of highly reactive structures on the defected surface, ultimately enhancing the efficiency of CL-POM.

Perovskite oxides hold significant potential in CL-POM due to their unique and tunable redox properties, high oxygen mobility and thermal stability [13,14,24]. $LaFeO_3$ (LFO) stands out as a

[1] Key Laboratory for Green Chemical Technology of Ministry of Education, School of Chemical Engineering & Technology, Tianjin University; Collaborative Innovation Center of Chemical Science and Engineering, Tianjin 300072, China
[2] Haihe Laboratory of Sustainable Chemical Transformations, Tianjin 300192, China
[3] National Industry-Education Platform of Energy Storage, Tianjin University, Tianjin 300350, China
[4] Joint School of National University of Singapore and Tianjin University, International Campus of Tianjin University, Fuzhou 350207, China
[5] Department of Chemistry, National University of Singapore, Science Drive 3, Singapore 117543, Republic of Singapore
* Corresponding author (email: zjzhao@tju.edu.cn)

© Science China Press 2024

promising OC for syngas production, achieving selectivities over 90% [18,30]. However, LFO faces limitations stemming from its low oxygen release capacity (percentage of removable oxygen atoms) and complex phase transition processes [25]. Therefore, $CaMnO_3$ is introduced as an OS due to its relatively high oxygen release capacity, suitable oxygen transport rates and tunable bulk properties [31–33]. However, the formation of inactive phases, $CaMn_2O_4$ (spinel structure) and Ca_2MnO_4 (Ruddlesden–Popper perovskite structure) after excessive reduction of $CaMnO_3$ dramatically reduces its oxygen release capacity. This impedes the replenishment of surface OVs by bulk oxygen atoms, ultimately leading to methane cracking and carbon deposition on the surface [33,34]. Doping with Sr^{2+} ions at the A-site has been identified as a strategy to mitigate this detrimental phase transition, thereby increasing the stability of $CaMnO_3$ [32,33].

$$CaMnO_3 \rightarrow CaMnO_{2.5} + \frac{1}{4}O_2, \quad (1)$$

$$6CaMnO_{2.5} \rightarrow 2CaMn_2O_{4-\delta} + 2Ca_2MnO_4 + (\delta - 0.5)O_2. \quad (2)$$

To achieve rate matching between surface reactions and bulk oxygen transport, we designed a composite OC ($LaFeO_{3-\delta}$/$Ca_{1-\eta}Sr_\eta MnO_3$) with a schematic structure depicted in Fig. S1, which allows for the precise adjustment of oxygen release capacity to maintain optimal active surface structures. This design significantly extends the CL-POM reaction process, facilitating a synergistic interplay between surface reactivity and oxygen transport performance. In this work, the determination of surface reaction rates was conducted using the steady-state approximation, taking into account the energy barriers of methane oxidation at two distinct active sites on the $LaFeO_{3-\delta}$ (121) defected surface, namely Fe-$O_4(O_v)$ and Fe-$O_3(O_v)_2$. Subsequently, bulk oxygen transport rates were determined based on oxygen migration energy barriers and OV concentrations, which are influenced by the covalency of Mn–O bonds and can be adjusted by varying Sr^{2+} doping concentrations. Furthermore, the introduction of Sr^{2+} ions also significantly inhibits the phase transition. Finally, we demonstrated that $LaFeO_{3-\delta}$/$Ca_{0.75}Sr_{0.25}MnO_3$ shows promising potential for achieving a rate matching between surface reactions and bulk oxygen transport.

THEORY AND METHODOLOGY

DFT calculations

All spin-polarized density functional theory (DFT) calculations were performed using the Vienna *ab initio* simulation package (VASP) [35]. The electron-nuclear interaction was described by the projector-augmented wave (PAW) method [36], and the electron density of the system was described by the Perdew–Burke–Ernzerhof (PBE) exchange-correlation functional [37]. For structural optimization and transition state determination, a cutoff energy of 600 eV was used [38], with the convergence criteria for energy and force set at 10^{-5} eV and 0.05 eV Å^{-1}, respectively. Transition state structures were determined using the climbing image nudged elastic band (CI-NEB) method [39] and the dimer method [40]. Each transition state structure was further validated through vibrational normal mode analysis to ensure the presence of only one imaginary frequency. In addition, the DFT-D3 correction [41] was employed to describe long-range van der Waals interactions. DFT + U [42] was used to accurately describe the strong d-electron interactions of transition metals (such as Fe and Mn), with a U_{eff} value of 4.3 eV for Fe in $LaFeO_3$ [43] and 3.0 eV for Mn in $CaMnO_3$ [44]. Both $LaFeO_3$ and $CaMnO_3$ exhibit an orthogonal perovskite structure (*Pnma*) with the G-type antiferromagnetic (G-AFM) configuration [45,46].

A single-layer slab of $LaFeO_{3-\delta}$ (121) with a p(1 × 1) cell and a three-layer slab of $CaMnO_3$ (121) with a p(1 × 1) cell were used to construct a periodic $LaFeO_{3-\delta}$/$CaMnO_3$ interface model (Fig. S1). The determination of this model is elaborated in Section 2 of the Supplementary information (Figs S2–S4). The bottom layer was fixed to simulate the bulk structure, while the top three layers were fully relaxed. To avoid the interaction between the slabs, a 15-Å vacuum layer was set in the z-direction. For the $LaFeO_{3-\delta}$/$CaMnO_3$ interface model, structural optimization and vibrational normal mode analysis of surface-adsorbed species were performed employing a 3 × 3 × 1 Monkhorst–Pack k-point grid, while a 5 × 5 × 1 Monkhorst–Pack k-point grid was used for electronic calculations. A series of 1 × 2 × 2 supercells were constructed to calculate the properties of bulk $CaMnO_3$, $CaMnO_{2.5}$ and $CaMn_2O_4$. Within these bulk supercells, 3 × 3 × 3 and 5 × 5 × 5 Monkhorst–Pack k-point grids were employed, with the former utilized for geometry optimization and phonon frequency calculations, and the latter for electronic calculations.

The formation energy of an OV (denoted as E_{O_v}) was calculated by the equation:

$$E_{O_v} = \left(E_{sto} + \frac{1}{2}E_{O_2}\right) - E_{def}, \quad (3)$$

where E_{sto} and E_{def} are the energies of the structure without or with an OV, respectively, and E_{O_2} is the corrected energy of an O_2 molecule calculated as $E_{O_2} = E_{DFT} - 1.36$ eV. E_{DFT} is the DFT energy of an O_2 molecule calculated using the generalized gradient approximation (GGA)-PBE functional. Due to the limitations of the GGA functional, E_{DFT} is significantly underestimated, necessitating an empirical correction of −1.36 eV [46].

The energy barrier (ΔE_a) for methane oxidation and oxygen migration was calculated using the equation:

$$\Delta E_a = E_{TS} - E_{IS}, \quad (4)$$

where E_{IS} and E_{TS} are the DFT energies of the initial state structure and the transition state structure in the elementary reaction, respectively.

The free energy barrier (ΔG_a) for methane oxidation and oxygen migration was calculated using the equation:

$$\Delta G_a = G_{TS} - G_{IS}, \quad (5)$$

where G_{IS} and G_{TS} are the free energies of the initial state structure and the transition state structure in the elementary reaction, respectively. The free energy (G) of a minimum or transition state structure, such as G_{IS} and G_{TS}, can be calculated by the equation:

$$G = E_{DFT} + E_{ZPE} + \Delta H - TS, \quad (6)$$

where E_{DFT} is the energy calculated by DFT, E_{ZPE} is the zero-point energy, ΔH is the enthalpy change from 0 K to T, T is the reaction temperature, and S is the entropy at T. The ΔH and S of free gas molecules were calculated from the standard thermodynamic data in the NIST database [47]. The ΔH and S of lattice oxygen atoms and surface-adsorbed species were obtained using

© Science China Press 2024

the harmonic oscillator approximation, with the former employing phonon frequencies and the latter employing vibration frequencies.

Modeling of a phase transition

The large-scale atomic simulation with neural network potential (LASP) software [48] was used to simulate the solid-solid phase transition process, employing the variable-cell double-ended surface walking (VC-DESW) method [49]. The independent random surface walking path sampling method (SSW) was used to perform global optimization from both the initial state and final state structures, respectively. The phase transition process from the initial state structure to the final state structure was identified at the intersection of these two search paths. The identified phase transition pathway was subsequently refined through more accurate DFT calculations, ultimately establishing the detailed phase transition pathway.

RESULTS AND DICUSSION

In this study, our focus is on using $LaFeO_{3-\delta}$ as the OC and $Ca_{1-\eta}Sr_{\eta}MnO_3$ as the OS. We were able to modulate the rate of bulk oxygen transport in $Ca_{1-\eta}Sr_{\eta}MnO_3$ by varying the Sr^{2+} doping concentration, thereby ensuring a match between the rates of surface reactions and bulk oxygen transport. Initially, we elucidated the reaction pathways of methane oxidation on the $LaFeO_{3-\delta}$ (121) defected surface to confirm the rate-determining step and the corresponding energy barrier. Following this, we calculated the oxygen migration barrier of $Ca_{1-\eta}Sr_{\eta}MnO_3$ and analyzed the effect of Sr^{2+} doping on oxygen formation and migration behavior. Based on these results, we evaluated the degree of rate matching between surface reactions and bulk oxygen transport in $LaFeO_{3-\delta}/Ca_{1-\eta}Sr_{\eta}MnO_3$. In addition, recognizing that the possibility of an undesired phase transition caused by continuous oxygen loss significantly impairs oxygen transport, we further investigated the effect of Sr^{2+} doping on mitigating this process. Ultimately, $LaFeO_{3-\delta}/Ca_{0.75}Sr_{0.25}MnO_3$ is demonstrated to be a potential candidate OC due to its excellent bulk oxygen transport rate and significant ability to inhibit the phase transition.

Methane oxidation on the $LaFeO_{3-\delta}$ (121) surface

To identify the highly active $LaFeO_{3-\delta}$ (121) defected surface that could form during the reaction process, we constructed a series of $LaFeO_{3-\delta}$ (121) slab models with different OV concentrations to simulate the process of continuous surface oxygen loss. The most stable surface structures with OV concentrations of 0%, 25%, 50%, and 75% are illustrated in Fig. S5. We then evaluated the activity of different surface sites on each defected surface by comparing their energy barriers for methane activation (Fig. S6), which is regarded as the rate-determining step [18,50]. The $LaFeO_{3-\delta}$ (121) surface with 50% OVs emerges as the catalytically active surface due to its relatively low methane activation energy. There are two active sites with different oxygen coordination configurations on this surface (Fig. 1b, d), namely Fe-$O_4(O_V)$ and Fe-$O_3(O_V)_2$, which exhibit a similar capacity for methane activation. The oxidation pathways of methane on these two active sites were systematically calculated (Fig. 1a, c), allowing for the subsequent determination of the rate of surface oxygen consumption using the steady-state approximation.

The three potential pathways for methane oxidation on Fe-$O_4(O_V)$ are illustrated in Fig. 1a. In these pathways, CH_4 and $*CH_x$ (x = 1, 2, 3) species undergo successive dehydrogenation on Fe-$O_4(O_V)$, ultimately yielding *C and *OH species. Subsequently, *CO species are formed when C* species combine with the terminal O atom (O_{1c}). These CO* species can either desorb directly, resulting in the formation of gaseous CO molecules, or react with lattice oxygen atoms migrating from the subsurface to the surface, resulting in the formation of CO_2* species. Given the strong bonding between *H atoms and lattice O atoms, it is observed that *H atoms prefer to migrate from O_{1c} to the bridging O site, O_{2c} (ΔG_a = 1.44 eV), rather than migrating to the OV site, O_V (ΔG_a = 2.09 eV). Note that the formations of H_2 and H_2O are parallel competing reactions. H*O_{1c} and H*O_{2c}, representing *H species adsorbed on O_{1c} and O_{2c}, respectively, favor the formation of H_2O (ΔG_a = 1.24 eV) over H_2 (ΔG_a = 3.11 eV). Therefore, the primary products of methane oxidation on Fe-$O_4(O_V)$ are CO and H_2O, with the migration of *H species from O_{1c} to O_{2c} identified as the rate-determining step.

In contrast, the formation of H_2 on Fe-$O_3(O_V)_2$ arises due to the reduced activity of oxygen sites, caused by the low-coordination environment of Fe-$O_3(O_V)_2$, as illustrated in Fig. 1c. This facilitates the dissociation of H*O species, promoting the migration of *H species from O_{2c} to O_v (ΔG_a = 0.74 eV) and subsequent H_2 generation (ΔG_a = 0.57 eV). The rate-determining step for methane oxidation on Fe-$O_3(O_V)_2$ involves the dehydrogenation of *CH species, resulting in *C and H*O_{2c} species (ΔG_a = 1.40 eV). The presence of OVs can hinder the formation of CO_2, as it becomes difficult for the *C species to coordinate with its two surrounding O atoms on Fe-$O_3(O_V)_2$. All energy data are available in Tables S1, S2, and transition state structures are shown in Figs S7, S8. Building on the insights gained from the two reaction pathways on Fe-$O_4(O_V)$ and Fe-$O_3(O_V)_2$ active sites, we further employed the steady-state approximation to calculate the rate of surface oxygen consumption, as elaborated in Section of Rate matching between surface reactions and bulk oxygen transport.

Oxygen migration behavior of $Ca_{1-\eta}Sr_{\eta}Mn_xO_y$

As surface oxygen atoms are continuously depleted during CL-POM, bulk oxygen atoms migrate from the bulk to the surface, driven by an oxygen concentration gradient between the bulk and the surface. This results in an increased loss of bulk oxygen, thereby triggering the phase transition of $CaMnO_3$. To understand the variation in oxygen release capacity and then to identify the impact of Sr^{2+} doping on oxygen migration, we investigated the oxygen migration behavior of three bulk structures formed during the phase transition: $CaMnO_3$, $CaMnO_{2.5}$ and $CaMn_2O_4$. $CaMnO_3$ and $CaMnO_{2.5}$ retain the favorable perovskite structure, while $CaMn_2O_4$ and Ca_2MnO_4 are formed with further reduction of $CaMnO_{2.5}$. The oxygen transport process after the phase transition was analyzed using the oxygen migration energy barrier in $CaMn_2O_4$, given its potential to significantly impede oxygen migration compared with Ca_2MnO_4 [51,52].

Upon examining the oxygen migration process of $LaFeO_{3-\delta}/CaMnO_3$ (Fig. 2a, b), we found that the migration energy barriers of the $LaFeO_{3-\delta}$ surface (ΔE_{mig} = 0.33 eV) and the $LaFeO_{3-\delta}/CaMnO_3$ interface (ΔE_{mig} = 0.32 eV) are significantly lower than those of bulk $CaMnO_3$ (ΔE_{mig} = 0.67 and 0.68 eV). This indicates that the oxygen migration in $CaMnO_3$ is the rate-determining step of the overall oxygen migration process. Therefore, it may be necessary to adjust the transport properties

© Science China Press 2024

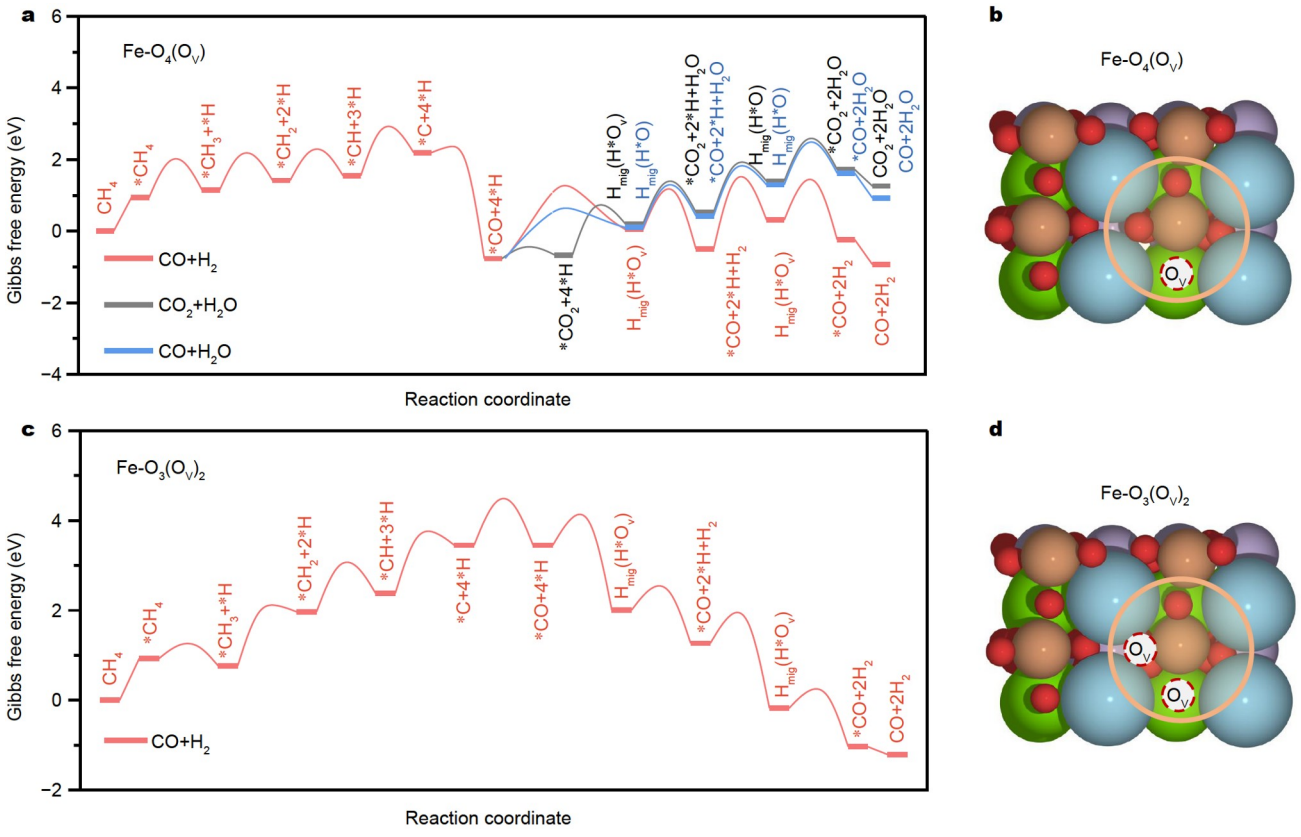

Figure 1 Reaction pathways of CL-POM on (a) Fe-$O_4(O_V)$ and (c) Fe-$O_3(O_V)_2$ active sites of the $LaFeO_{3-\delta}$ (121) defected surface. Schematic structures of (b) Fe-$O_4(O_V)$ and (d) Fe-$O_3(O_V)_2$.

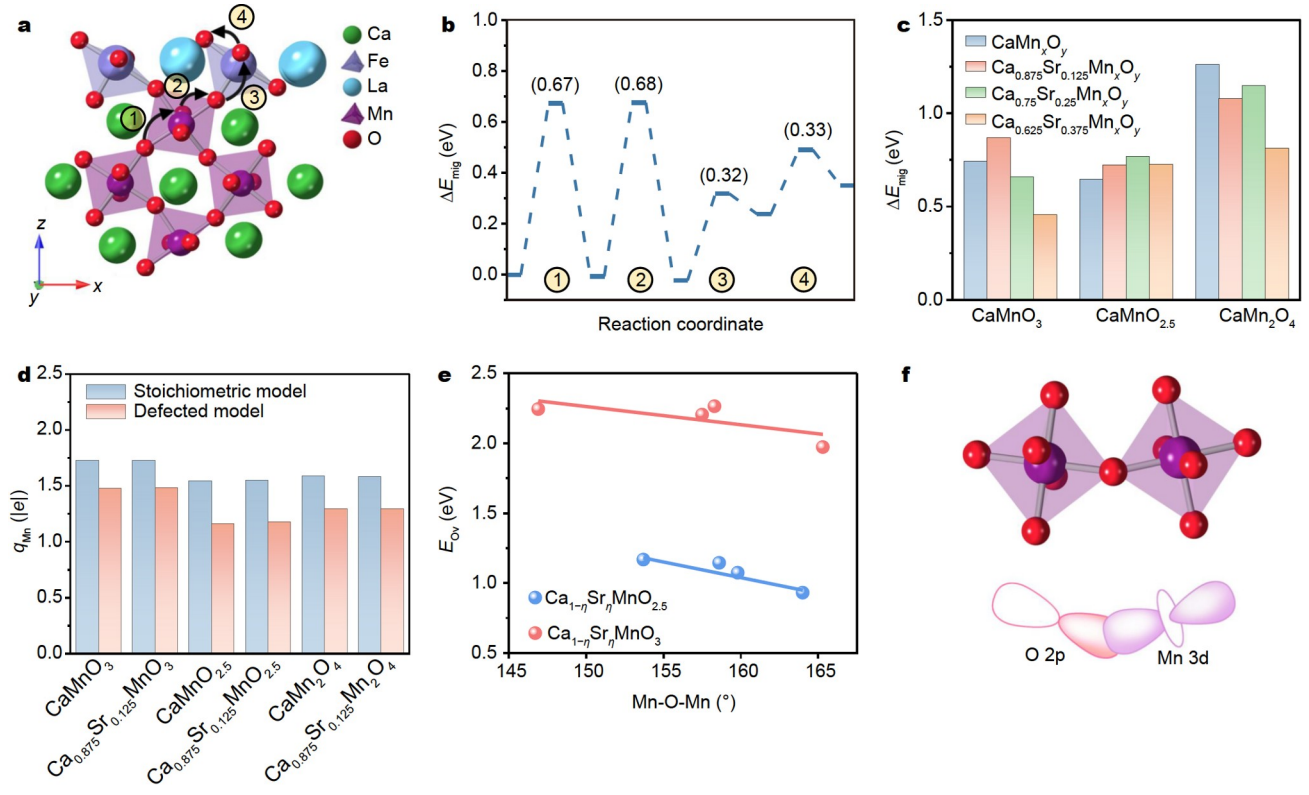

Figure 2 (a) Schematic pathways and (b) the corresponding energy barriers of one bulk O atom migration from the bulk to the surface in $LaFeO_{3-\delta}$/$CaMnO_3$. (c) Migration energy barriers, (d) the Bader charge of Mn and (e) OV formation energies in $CaMn_xO_y$ and Sr-doped $Ca_{1-\eta}Sr_\eta Mn_xO_y$. (f) Schematic diagram of the M–O interaction.

© Science China Press 2024

of bulk $CaMnO_3$ to synchronize the surface reaction rate with the bulk oxygen transport rate.

Next, we calculated the oxygen migration energy barriers of $CaMn_xO_y$ to shed light on the variation in the intrinsic oxygen release capacity of different phases. As shown in Fig. 2c, $CaMn_2O_4$ exhibits a significantly higher migration energy barrier compared with $CaMnO_3$ and $CaMnO_{2.5}$, both of which retain the favorable perovskite structure. With Sr^{2+} doping at the A-site, OV preferentially occupies the nearest-neighbor position of MnO_x near a Sr^{2+} ion (Figs S9–S11). To elucidate the effect of Sr^{2+} doping on the oxygen migration capacity, we further investigated the electronic and geometric structures of $CaMn_xO_y$ and $Ca_{1-\eta}Sr_\eta Mn_xO_y$. As illustrated in Fig. 2c, the introduction of Sr^{2+} ions leads to a change in the migration energy barrier. However, when Sr^{2+} ions are doped into the $CaMn_xO_y$ lattice, the average charges of Mn and O remain stable regardless of the presence of an OV (Fig. 2d, Fig. S12 and Table S3). This indicates that Sr^{2+} doping may not significantly alter the electronic structure of MnO_x. Notably, a linear relationship between the formation energy of OVs and the Mn–O–Mn bond angle was observed for $Ca_{1-\eta}Sr_\eta MnO_3$ and $Ca_{1-\eta}Sr_\eta MnO_{2.5}$ (Fig. 2e). According to molecular orbital theory, the enlarged Mn–O–Mn bond angle would increase the spatial overlap between Mn 3d and O 2p orbitals, thereby enhancing the covalency of Mn–O bonds and promoting the formation of OVs (Fig. 2f). In this context, due to the large Mn–O–Mn bond angle, $Ca_{0.75}Sr_{0.25}MnO_3$ emerges as a candidate OS, given its lowest E_{O_v} (Table S4), which may exhibit a rapid oxygen transport rate and relatively large oxygen loss. Consequently, the primary impact of Sr^{2+} doping on oxygen transport and OV formation is likely to be due to the modulation of MnO_x distortions.

Rate matching between surface reactions and bulk oxygen transport

To identify the optimal structure of $Ca_{1-\eta}Sr_\eta Mn_xO_y$ that achieves a balance between the rates of surface reactions and bulk oxygen transport, we examined these rates, quantified as the amount of oxygen atoms consumed on the surface and transferred from the bulk to the surface per unit time, respectively (see Section 1.2 and 1.3 of the Supplementary information). The concentration of OVs in $Ca_{1-\eta}Sr_\eta Mn_xO_y$ was calculated using the equilibrium method [53] (see Section 1.3 of the Supplementary information). These results, depicted in Fig. 3a, align with the orders of magnitude reported in previous studies [53]. As the Sr^{2+} concentration increases, the OV concentration in $Ca_{1-\eta}Sr_\eta Mn_xO_y$ initially rises and then declines, mirroring the trend of E_{O_v} influenced by the change in Mn–O–Mn bond angle. These results further substantiate the conclusion that a larger Mn–O–Mn bond angle fosters the formation of OVs, thereby facilitating the release of more bulk oxygen atoms.

Furthermore, we found that the oxygen transport rate is dependent on both the oxygen transport coefficient and OV concentration. Due to the low migration energy barrier (ΔG_{mig} = 0.61 eV) and high transport coefficient (D_O = 2.29×10^{-17} m^2 s^{-1}, Table S5), $Ca_{0.625}Sr_{0.375}MnO_3$ exhibits the highest oxygen transport capacity despite having a lower OV concentration compared with $Ca_{1-\eta}Sr_\eta MnO_3$. Conversely, the high migration energy barrier of $Ca_{0.875}Sr_{0.125}MnO_3$ (ΔG_{mig} = 1.01 eV) results in a low transport coefficient (D_O = 1.27×10^{-18} m^2 s^{-1}, Table S5), hindering the oxygen transport, even though its OV concentration is higher than those of $CaMnO_3$ and $Ca_{0.625}Sr_{0.375}MnO_3$. By comparing the bulk oxygen transport rate in $Ca_{1-\eta}Sr_\eta Mn_xO_y$ with the surface reaction rate, we determined that both $Ca_{0.75}Sr_{0.25}MnO_3$ and $Ca_{0.625}Sr_{0.375}MnO_3$ have the potential to maintain favorable structures of the $LaFeO_{3-\delta}$ (121) defected surface (Fig. 3b), as the rates of surface oxygen consumption and replenishment are of the same magnitude. Therefore, these two oxides are promising candidates for achieving rate matching between surface reactions and bulk oxygen transport.

Additionally, we found that the oxygen transport rate of $Ca_{1-\eta}Sr_\eta MnO_{2.5}$ is significantly lower than the surface reaction rate. Given the similar perovskite structures of $Ca_{1-\eta}Sr_\eta MnO_{2.5}$ and $Ca_{1-\eta}Sr_\eta MnO_3$, the former can be viewed as the latter with 1/6 reduction in oxygen. Consequently, the amount of OVs in $Ca_{1-\eta}Sr_\eta MnO_{2.5}$, which could potentially aid in oxygen transport,

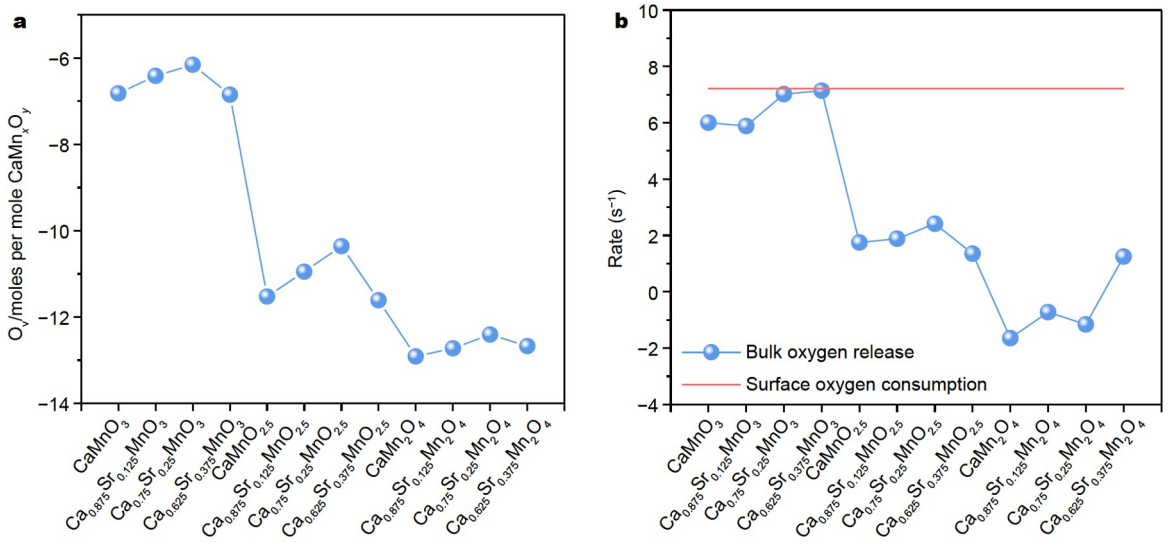

Figure 3 (a) Equilibrium OV concentrations and (b) the rate matching between surface oxygen consumption and bulk oxygen transport of $CaMn_xO_y$ and $Ca_{1-\eta}Sr_\eta Mn_xO_y$.

© Science China Press 2024

may exceed the amount calculated by the equilibrium method. This could lead to a higher oxygen transport rate of $Ca_{1-\eta}Sr_{\eta}MnO_{2.5}$. However, when $Ca_{1-\eta}Sr_{\eta}Mn_2O_4$ is used as the OS, due to its low oxygen transport rate and the lack of additional bulk OVs as seen in $Ca_{1-\eta}Sr_{\eta}MnO_{2.5}$, methane cracking may occur on the $LaFeO_{3-\delta}$ (121) defected surface, rather than methane oxidation.

The effect of Sr^{2+} doping on the phase transition

The formation of $Ca_{1-\eta}Sr_{\eta}Mn_2O_4$ with low oxygen transport rates may lead to excessive reduction of the $LaFeO_{3-\delta}$ surface and subsequent catalyst deactivation, thereby impeding the CL-POM process [14]. Thus, we subsequently investigated the effect of Sr^{2+} doping on inhibiting the formation of $Ca_{1-\eta}Sr_{\eta}Mn_2O_4$, that is, the phase transition from $Ca_{1-\eta}Sr_{\eta}MnO_{2.5}$ to $Ca_{1-\eta}Sr_{\eta}Mn_2O_4$. To establish the initial structure with the same stoichiometry as $Ca_{1-\eta}Sr_{\eta}Mn_2O_4$, we systematically removed 8 Ca atoms and 8 O atoms in a step-by-step manner. We then conducted extensive searches using global optimization, involving over 12,000 structures, from which the most stable structure for each distinct Sr^{2+} doping concentration was selected as the initial structure of the phase transition (the detailed process and results are illustrated in Section 9 of the Supplementary information, Figs S13–15).

As shown in Fig. 4, the phase transition of $Ca_{1-\eta}Sr_{\eta}MnO_{2.5}$ involves three stages: oxygen atom migration, spinel structure formation, and lattice expansion. Notably, the energy barrier of oxygen migration is higher compared with the other two stages, possibly due to the cell contraction (Fig. 4e). Comparing pure $CaMnO_{2.5}$ with $Ca_{0.875}Sr_{0.125}MnO_{2.5}$, the introduction of a small amount of Sr^{2+} ions alleviates cell contraction, resulting in a larger spatial domain for oxygen migration and thus a lower migration energy barrier (Fig. 4b). However, the oxygen migration capacity of $Ca_{0.75}Sr_{0.25}MnO_{2.5}$ and $Ca_{0.625}Sr_{0.375}MnO_{2.5}$ is inferior to that of $CaMnO_{2.5}$ (Fig. 4c, d), which is caused by the reduction of the oxygen migration space due to the higher concentration of Sr^{2+} ions. After some oxygen atoms migrate to adjacent vacancies, the arrangement of atoms closely resembled that of the spinel structure. The lattice structure was then optimized, specifically allowing an increase in the lattice constant along the *Z*-axis, to obtain a reasonable spinel-like structure. Finally, the cell was subjected to further lattice optimization and atomic relaxation to form a stable spinel structure. Detailed energy data are available in Table S6. Clearly, the introduction of Sr^{2+} ions exerts a significant impact on the oxygen transport, primarily by changing the geometric space for oxygen migration, consequently leading to the variation of the transition energy barrier.

According to our calculated oxygen transport rate, both $Ca_{0.75}Sr_{0.25}MnO_3$ and $Ca_{0.625}Sr_{0.375}MnO_3$ contribute to maintaining the $LaFeO_{3-\delta}$ (121) defected surface, but the former exhibits a higher phase transition energy barrier. Therefore, we can conclude that $Ca_{0.75}Sr_{0.25}MnO_3$ is a potential OS, due to its commendable oxygen release capacity and proficient ability to inhibit the phase transition.

CONCLUSIONS

In summary, both Fe-$O_4(O_V)$ and Fe-$O_3(O_V)_2$ have been identified as active sites on the $LaFeO_{3-\delta}$ (121) defected surface. Fe-$O_4(O_V)$ shows a preference for generating CO and H_2O (ΔG_a = 1.44 eV), while Fe-$O_3(O_V)_2$ predominantly produces CO and H_2 (ΔG_a = 1.40 eV). The introduction of Sr^{2+} ions serves to increase the Mn–O–Mn bond angle, thereby enhancing the covalency of Mn–O bonds and consequently promoting the formation of OVs. Remarkably, $CaMnO_3$ with 25% Sr^{2+} dopant achieves a bulk oxygen transport rate that is comparable to the surface reaction rate and effectively suppresses the phase transition. As a result, $LaFeO_{3-\delta}/Ca_{0.75}Sr_{0.25}MnO_3$ is proposed as a

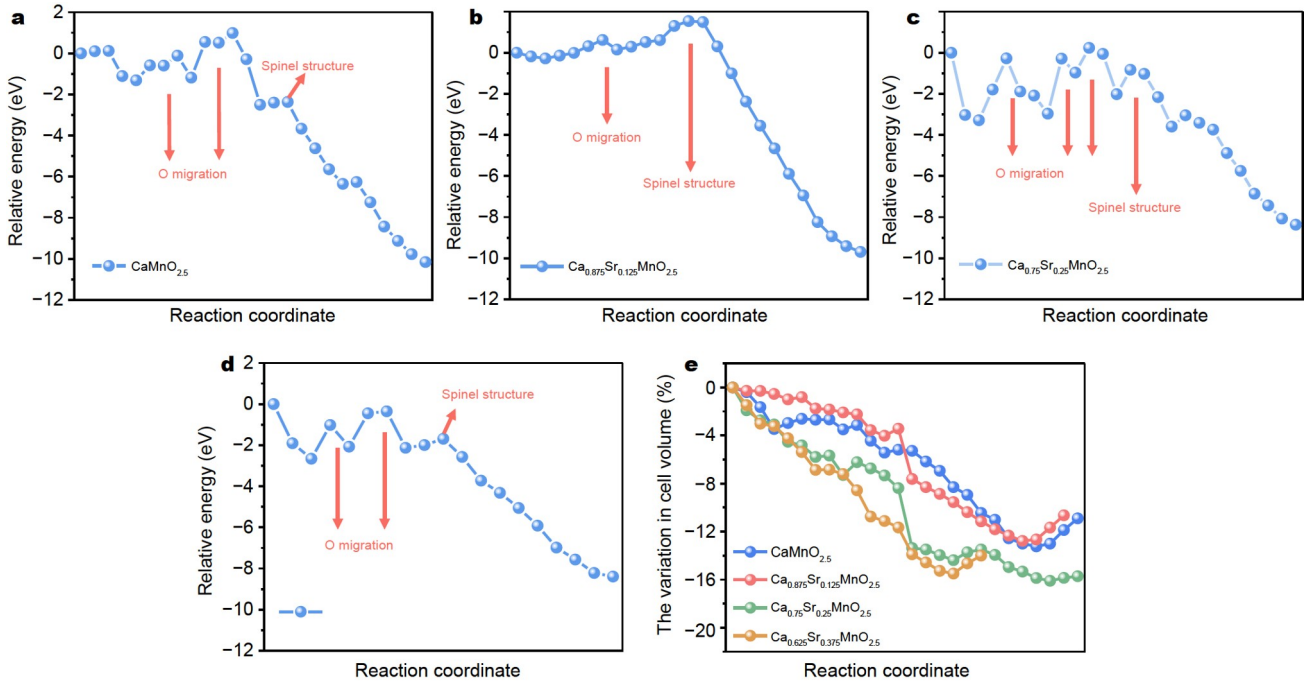

Figure 4 Phase transition simulation of (a) $CaMnO_{2.5}$, (b) $Ca_{0.875}Sr_{0.125}MnO_{2.5}$, (c) $Ca_{0.75}Sr_{0.25}MnO_{2.5}$, and (d) $Ca_{0.625}Sr_{0.375}MnO_{2.5}$. (e) Variation in cell volume during the phase transition.

© Science China Press 2024

potential candidate for CL-POM. These findings provide insight into addressing the critical challenge in CL-POM by modulating the active surface structures through the manipulation of the bulk oxygen transport capacity, which may have implications for future OC design for chemical looping.

Received 27 November 2023; accepted 4 March 2024; published online 25 March 2024

1 Spivey JJ, Hutchings G. Catalytic aromatization of methane. Chem Soc Rev, 2014, 43: 792–803
2 Schwarz H. Chemistry with methane: Concepts rather than recipes. Angew Chem Int Ed, 2011, 50: 10096–10115
3 Zhang Y, Sahir AH, Tan ECD, *et al.* Economic and environmental potentials for natural gas to enhance biomass-to-liquid fuels technologies. Green Chem, 2018, 20: 5358–5373
4 Khodakov AY, Chu W, Fongarland P. Advances in the development of novel cobalt Fischer–Tropsch catalysts for synthesis of long-chain hydrocarbons and clean fuels. Chem Rev, 2007, 107: 1692–1744
5 Aramouni NAK, Touma JG, Tarboush BA, *et al.* Catalyst design for dry reforming of methane: Analysis review. Renew Sustain Energy Rev, 2018, 82: 2570–2585
6 Yu Y, Lei H, Wang L, *et al.* Mechanisms of transforming CH_x to CO on Ni(111) surface by density functional theory. Trans Tianjin Univ, 2019, 25: 330–339
7 Kondratenko VA, Berger-Karin C, Kondratenko EV. Partial oxidation of methane to syngas over γ-Al_2O_3-supported Rh nanoparticles: Kinetic and mechanistic origins of size effect on selectivity and activity. ACS Catal, 2014, 4: 3136–3144
8 Choudhary T, Choudhary V. Energy-efficient syngas production through catalytic oxy-methane reforming reactions. Angew Chem Int Ed, 2008, 47: 1828–1847
9 Li Z, Liu R, Liu R, *et al.* Novel method for preparing a carbon nanotube-supported cobalt catalyst for Fischer–Tropsch synthesis: Hydrogen dielectric-barrier discharge plasma. Trans Tianjin Univ, 2017, 23: 20–25
10 Calderone VR, Shiju NR, Ferré DC, *et al.* Bimetallic catalysts for the Fischer–Tropsch reaction. Green Chem, 2011, 13: 1950–1959
11 Li K, Wang H, Wei Y, *et al.* Direct conversion of methane to synthesis gas using lattice oxygen of CeO_2–Fe_2O_3 complex oxides. Chem Eng J, 2010, 156: 512–518
12 Tang M, Xu L, Fan M. Progress in oxygen carrier development of methane-based chemical-looping reforming: A review. Appl Energy, 2015, 151: 143–156
13 Zhang X, Liu R, Liu T, *et al.* Redox catalysts for chemical looping methane conversion. Trends Chem, 2023, 5: 512–525
14 Zhu X, Li K, Neal L, *et al.* Perovskites as geo-inspired oxygen storage materials for chemical looping and three-way catalysis: A perspective. ACS Catal, 2018, 8: 8213–8236
15 Zhu X, Imtiaz Q, Donat F, *et al.* Chemical looping beyond combustion—A perspective. Energy Environ Sci, 2020, 13: 772–804
16 Ruan C, Huang ZQ, Lin J, *et al.* Synergy of the catalytic activation on Ni and the CeO_2–TiO_2/$Ce_2Ti_2O_7$ stoichiometric redox cycle for dramatically enhanced solar fuel production. Energy Environ Sci, 2019, 12: 767–779
17 Zhang X, Pei C, Chang X, *et al.* FeO_6 octahedral distortion activates lattice oxygen in perovskite ferrite for methane partial oxidation coupled with CO_2 splitting. J Am Chem Soc, 2020, 142: 11540–11549
18 Yang J, Bjørgum E, Chang H, *et al.* On the ensemble requirement of fully selective chemical looping methane partial oxidation over La-Fe-based perovskites. Appl Catal B-Environ, 2022, 301: 120788
19 Mihai O, Chen D, Holmen A. Chemical looping methane partial oxidation: The effect of the crystal size and O content of $LaFeO_3$. J Catal, 2012, 293: 175–185
20 Chang H, Bjørgum E, Mihai O, *et al.* Effects of oxygen mobility in La–Fe-based perovskites on the catalytic activity and selectivity of methane oxidation. ACS Catal, 2020, 10: 3707–3719
21 Jiang B, Li L, Zhang Q, *et al.* Iron–oxygen covalency in perovskites to dominate syngas yield in chemical looping partial oxidation. J Mater Chem A, 2021, 9: 13008–13018
22 Zhao K, Chen J, Li H, *et al.* Investigation of the relationship between electronic properties and reactivity of 3DOM $LaFe_{1-x}Co_xO_3$ for methane reforming to produce syngas. Int J Energy Res, 2019, 43: er.4736
23 Neal LM, Shafiefarhood A, Li F. Dynamic methane partial oxidation using a Fe_2O_3@$La_{0.8}Sr_{0.2}FeO_{3-\delta}$ core–shell redox catalyst in the absence of gaseous oxygen. ACS Catal, 2014, 4: 3560–3569
24 Zhang L, Xu W, Wu J, *et al.* Identifying the role of A-site cations in modulating oxygen capacity of iron-based perovskite for enhanced chemical looping methane-to-syngas conversion. ACS Catal, 2020, 10: 9420–9430
25 Dai X, Cheng J, Li Z, *et al.* Reduction kinetics of lanthanum ferrite perovskite for the production of synthesis gas by chemical-looping methane reforming. Chem Eng Sci, 2016, 153: 236–245
26 Mihai O, Chen D, Holmen A. Catalytic consequence of oxygen of lanthanum ferrite perovskite in chemical looping reforming of methane. Ind Eng Chem Res, 2010, 50: 2613–2621
27 Chen S, Luo R, Zhao ZJ, *et al.* Concerted oxygen diffusion across heterogeneous oxide interfaces for intensified propane dehydrogenation. Nat Commun, 2023, 14: 2620
28 Zheng Y, Li K, Wang H, *et al.* Designed oxygen carriers from macroporous $LaFeO_3$ supported CeO_2 for chemical-looping reforming of methane. Appl Catal B-Environ, 2017, 202: 51–63
29 Zeng L, Cheng Z, Fan JA, *et al.* Metal oxide redox chemistry for chemical looping processes. Nat Rev Chem, 2018, 2: 349–364
30 Dai XP, Li J, Fan JT, *et al.* Synthesis gas generation by chemical-looping reforming in a circulating fluidized bed reactor using perovskite $LaFeO_3$-based oxygen carriers. Ind Eng Chem Res, 2012, 51: 11072–11082
31 Kim J, Yin X, Tsao KC, *et al.* $Ca_2Mn_2O_5$ as oxygen-deficient perovskite electrocatalyst for oxygen evolution reaction. J Am Chem Soc, 2014, 136: 14646–14649
32 Bulfin B, Vieten J, Starr DE, *et al.* Redox chemistry of $CaMnO_3$ and $Ca_{0.8}Sr_{0.2}MnO_3$ oxygen storage perovskites. J Mater Chem A, 2017, 5: 7912–7919
33 Galinsky N, Sendi M, Bowers L, *et al.* $CaMn_{1-x}B_xO_{3-\delta}$ (B = Al, V, Fe, Co, and Ni) perovskite based oxygen carriers for chemical looping with oxygen uncoupling (CLOU). Appl Energy, 2016, 174: 80–87
34 Molinari M, Tompsett DA, Parker SC, *et al.* Structural, electronic and thermoelectric behaviour of $CaMnO_3$ and $CaMnO_{(3-\delta)}$. J Mater Chem A, 2014, 2: 14109–14117
35 Kresse G, Furthmüller J. Efficiency of *ab-initio* total energy calculations for metals and semiconductors using a plane-wave basis set. Comput Mater Sci, 1996, 6: 15–50
36 Kresse G, Joubert D. From ultrasoft pseudopotentials to the projector augmented-wave method. Phys Rev B, 1999, 59: 1758–1775
37 Perdew JP, Burke K, Ernzerhof M. Generalized gradient approximation made simple. Phys Rev Lett, 1996, 77: 3865–3868
38 Zheng YS, Zhang M, Li Q, *et al.* Electronic origin of oxygen transport behavior in La-based perovskites: A density functional theory study. J Phys Chem C, 2019, 123: 275–290
39 Henkelman G, Uberuaga BP, Jónsson H. A climbing image nudged elastic band method for finding saddle points and minimum energy paths. J Chem Phys, 2000, 113: 9901–9904
40 Henkelman G, Jónsson H. Improved tangent estimate in the nudged elastic band method for finding minimum energy paths and saddle points. J Chem Phys, 2000, 113: 9978–9985
41 Grimme S, Antony J, Ehrlich S, *et al.* A consistent and accurate *ab initio* parametrization of density functional dispersion correction (DFT-D) for the 94 elements H-Pu. J Chem Phys, 2010, 132: 154104
42 Rohrbach A, Hafner J, Kresse G. Electronic correlation effects in transition-metal sulfides. J Phys-Condens Matter, 2003, 15: 979–996
43 Mosey NJ, Liao P, Carter EA. Rotationally invariant *ab initio* evaluation of Coulomb and exchange parameters for DFT + *U* calculations. J Chem Phys, 2008, 129: 014103
44 Hong J, Stroppa A, Íñiguez J, *et al.* Spin-phonon coupling effects in transition-metal perovskites: A DFT + *U* and hybrid-functional study. Phys Rev B, 2012, 85: 054417
45 He J, Franchini C. Screened hybrid functional applied to $3d^0 \rightarrow 3d^8$

 © Science China Press 2024

transition-metal perovskites $LaMO_3$ (M = Sc–Cu): Influence of the exchange mixing parameter on the structural, electronic, and magnetic properties. Phys Rev B, 2012, 86: 235117
46 Wang L, Maxisch T, Ceder G. Oxidation energies of transition metal oxides within the GGA + *U* framework. Phys Rev B, 2006, 73: 195107
47 NIST-JANAF Thermochemical Tables, NIST Standard Reference Database 13, Last Update to Data Content: 1998, DOI: 10.18434/T42S31, https://janaf.nist.gov/
48 Gao Q, Hao J, Qiu Y, *et al.* Electronic and geometric factors affecting oxygen vacancy formation on CeO_2(111) surfaces: A first-principles study from trivalent metal doping cases. Appl Surf Sci, 2019, 497: 143732
49 Shang C, Liu ZP. Stochastic surface walking method for structure prediction and pathway searching. J Chem Theor Comput, 2013, 9: 1838–1845
50 Wei J, Iglesia E. Structural and mechanistic requirements for methane activation and chemical conversion on supported iridium clusters. Angew Chem Int Ed, 2004, 43: 3685–3688
51 Zhang W, Sun Y, Deng H, *et al.* Dielectric polarization in inverse spinel-structured Mg_2TiO_4 coating to suppress oxygen evolution of Li-rich cathode materials. Adv Mater, 2020, 32: 2000496
52 Xu S, Jacobs R, Morgan D. Factors controlling oxygen interstitial diffusion in the Ruddlesden–Popper oxide $La_{2-x}Sr_xNiO_{4+\delta}$. Chem Mater, 2018, 30: 7166–7177
53 Ritzmann AM, Pavone M, Muñoz-García AB, *et al. Ab initio* DFT+*U* analysis of oxygen transport in $LaCoO_3$: The effect of Co^{3+} magnetic states. J Mater Chem A, 2014, 2: 8060–8074

Acknowledgements We thank Prof. Lyudmila Moskaleva for the discussion on the manuscript. This work was supported by the National Key R&D Program of China (2022YFE0102000), the National Natural Science Foundation of China (22121004 and U22A20409), Haihe Laboratory of Sustainable Chemical Transformations, the Program of Introducing Talents of Discipline to Universities (BP0618007) and the XPLORER PRIZE for financial support. We also acknowledge generous computing resources at High Performance Computing Center of Tianjin University.

Author contributions Yang T performed the calculations and drafted the manuscript. Luo R, Shi X, and Wu S assisted in the analysis of the calculated results. Zhang X and Pei C contributed to useful discussion. Zhao ZJ and Gong J designed and supervised the project. All authors participated in general discussion and the manuscript revision.

Conflict of interest The authors declare that they have no conflict of interest.

Supplementary information Supporting data are available in the online version of the paper.

Tingting Yang received her BSc degree in chemical engineering and technology from the South China University of Technology. She is currently an MSc candidate at the School of Chemical Engineering and Technology, Tianjin University. Her current interest focuses on theoretical studies of thermocatalytic reactions.

Zhi-Jian Zhao received his BSc and MSc degrees in chemistry from Zhejiang University and his PhD degree from Technische Universität München. He then worked as a postdoctoral fellow with Prof. Greeley in Purdue University, and with Dr. Studt and Prof. Nørskov at Stanford University. Currently, he holds a professorship at Tianjin University. His current research focuses on mechanistic studies on heterogeneous catalysts using multi-scaling simulation methods.

调控氧传输以实现甲烷化学链部分氧化表面和体相速率的匹配

杨婷婷[1], 罗冉[1], 石向成[1,5], 张先华[1], 吴仕灿[1], 裴春雷[1], 赵志坚[1,2,3*], 巩金龙[1,2,3,4,5]

摘要 甲烷化学链部分氧化(CL-POM)是一种有前景的合成气生产技术, 具有高选择性和低爆炸风险的优势. 然而, 开发性能优异、可持续释氧的金属载氧体仍然面临挑战. 为此, 本研究设计了一种复合载氧体($LaFeO_{3-\delta}/Ca_{1-\eta}Sr_\eta MnO_3$), 通过调控$Ca_{1-\eta}Sr_\eta MnO_3$的氧扩散来维持$LaFeO_{3-\delta}$ (121)缺陷表面的活性结构, 从而提升了CL-POM的活性和选择性. 理论计算结果表明, 甲烷在$LaFeO_{3-\delta}$ (121)缺陷表面上的反应活性位点主要是Fe-$O_4(O_V)$和Fe-$O_3(O_V)_2$, 它们表现出相近的反应能垒(ΔG_a = 1.44 和 1.40 eV). 氧扩散系数和表面反应速率常数分别由体相氧迁移能垒和表面反应能垒确定, 进而计算得到体相氧扩散和表面反应的速率, 用以评估两者的匹配程度. 最后, 本研究证实了$LaFeO_{3-\delta}/Ca_{0.75}Sr_{0.25}MnO_3$是一种有潜力的CL-POM载氧体, 其能够实现体相氧扩散速率与表面氧消耗速率的合理匹配, 并有效地抑制不利的相变过程.

 © Science China Press 2024